Chemical Science

ROYAL SOCIETY OF CHEMISTRY

EDGE ARTICLE

View Article Online
View Journal | View Issue

Open Access Article. Published on 27 August 2024. Downloaded on 2/7/2026 1:52:40 PM.
This article is licensed under a Creative Commons Attribution-NonCommercial 3.0 Unported Licence.

Check for updates

Cite this: *Chem. Sci.*, 2024, **15**, 15717

All publication charges for this article have been paid for by the Royal Society of Chemistry

Exclusive generation of a superoxide radical by a porous aromatic framework for fast photocatalytic decontamination of mustard gas simulant in room air†

Jian Song,‡ Hengtao Lei,‡ Yuhui Zhai, Zilong Dou, Yongyue Ding, Xueyan Han, Fengchao Cui, Yuyang Tian * and Guangshan Zhu *

Mustard gas and other chemical warfare agents (CWAs) are a global threat to public security, arising from unpredictable emergencies and chemical spill accidents. So far, photocatalysts such as metal clusters, polyoxometalates and porous solids have been exploited for oxidative degradation of mustard gas, commonly with $^1O_2$ as reactive species. However, the production of $^1O_2$ is oxygen-dependent and requires a high oxygen concentration to sustain the detoxication process. For safety and operation process considerations, it is always preferable to rapidly detoxify dangerous chemicals in the atmosphere of room air. In this work, a porous aromatic framework, **PAF-68**, was synthesized as a metal-free photocatalyst. In the presence of **PAF-68**, fast detoxication occurred in typical room air atmosphere. The half-life ($t_{1/2}$) for the complete conversion of mustard gas simulant to nontoxic product in room air was only 1.7 min, which is comparable to the performance in pure oxygen, surpassing that of any other porous photocatalysts. It was found that $^{\bullet}O_2^-$ rather than $^1O_2$ is the predominant reactive species initiated by **PAF-68** for mustard gas detoxication. Unlike the formation of $^1O_2$ which prefers the environment of pure oxygen, generation of the $^{\bullet}O_2^-$ is an oxygen-independent process. It is suggested that amorphous PAFs possess low exciton binding energy and long decay lifetime, which facilitate the generation of $^{\bullet}O_2^-$, and this offers a general design strategy to detoxifying chemical warfare agents under real-world conditions.

Received 9th July 2024
Accepted 27th August 2024

DOI: 10.1039/d4sc04551c

rsc.li/chemical-science

Introduction

CWAs are a global threat because of their strong lethality, ready availability, and diverse exposure pathways.[1,2] Among them, mustard gas (HD) is a typical representative of corrosive poisons, and it is widely regarded as a historically significant chemical weapon, referred to as the "king of poisons" for its potent corrosiveness, chemical stability, long-lasting effectiveness, and especially difficult detoxication.[3] Compared to other detoxifying approaches such as dehydrochlorination and hydrolysis, oxidation of HD is especially regarded as more promising for its fast conversion and innocuous products. Among the oxidation processes, photocatalytic oxidation driven by light, as the source of energy, is the most attractive due to its efficiency, sustainability and ease of operation.[4] In pioneering research, Farha *et al.* used the metal organic framework (MOF) PCN-222 as a photocatalyst for mustard gas simulant detoxication. In an atmosphere of pure oxygen and under LED light irradiation, a mustard gas simulant, 2-chloroethyl ethyl sulfide (CEES), was selectively oxidized to its nontoxic product 2-chloroethyl ethyl sulfoxide (CEESO) with a half-life ($t_{1/2}$) of 13 min.[5] There has since been extensive work on the design of photocatalysts to faster convert mustard gas and its simulants.[6–8] With regard to oxidation, selective conversion of mustard gas to its sulfoxide product is preferred because over-oxidation results in the production of a sulfone compound, which is as toxic as HD itself.[9] Besides their demanding selectivity, catalysts and oxidants should be carefully selected to achieve fast detoxication. However, almost all currently reported photocatalytic reactions require pure oxygen, or even more dangerously, hydrogen peroxide as oxidants, because the reactive oxygen species (ROS) usually relies on the concentration of the oxidants.[10,11] Despite singlet oxygen ($^1O_2$) being commonly used to selectively oxidize CEES to CEESO, a high concentration of oxygen molecules is needed to ensure a viable oxidation rate, due to the oxygen-dependent feature of $^1O_2$ formation.[12,13] Consequently, under an atmosphere of typical room air, with an oxygen partial pressure around 20%, the rate

Key Laboratory of Polyoxometalate and Reticular Material Chemistry of Ministry of Education, Faculty of Chemistry, Northeast Normal University, Changchun, Jilin 130024, China. E-mail: tianyy100@nenu.edu.cn; zhugs@nenu.edu.cn

† Electronic supplementary information (ESI) available. See DOI: https://doi.org/10.1039/d4sc04551c

‡ These authors contributed equally to this work.

Open Access Article. Published on 27 August 2024. Downloaded on 2/7/2026 1:52:40 PM. This article is licensed under a Creative Commons Attribution-NonCommercial 3.0 Unported Licence.

of CEES oxidation by $^1O_2$ is significantly reduced.[5,14] In real-world conditions, carrying pure oxygen or even explosive hydrogen peroxide as oxidants is difficult and risky. Therefore, the design and synthesis of photocatalysts for rapid degradation of CEES in an atmosphere of room air is an urgent goal of current research.

Porous solids, including metal–organic frameworks (MOFs) and covalent organic frameworks (COFs), have exhibited significant performance as photocatalysts owing to their massive accessible active sites and adjustable energy band structures.[15–17] However, in practice, most of these materials serving as heterogeneous catalysts face the challenge of weak stability. In contrast, porous aromatic frameworks (PAFs) are a class of porous materials entirely constructed from organic building units, where the building units are linked *via* stable carbon–carbon covalent bonds.[18,19] Due to their structural features, PAFs possess numerous accessible internal surfaces, a stable framework, and sub-nanometer-scaled pores, which are used as functional materials for adsorption,[20] separation,[20,21] catalysis,[22] and as solid electrolytes,[23,24] to name but a few. Apart from their exceptional stability, the physical and chemical properties of PAFs can be readily designed and modulated by the screening and modification of suitable building units.[25] Therefore, the development of photoactive PAFs for ROS-related processes would be an alluring option.

Herein, a photoactive PAF (**PAF-68**) with high specific surface area and high stability was successfully synthesized, with tris(4-ethynylphenyl)amine (**EPA**) and *meso*-tetra(*p*-bromophenyl) porphyrin (**TBPP**) as building units (Fig. 1). **PAF-68** showed good efficacy for the aerobic oxidation of mustard gas simulant. In humid O_2, CEES was completely converted into the nontoxic CEESO with a half-life of 1.5 min. In an atmosphere of room air, regardless of the low oxygen partial pressure and the humidity, the half-life of the conversion of CEES to CEESO by **PAF-68** reached an ultrafast pace of 1.7 min, which is quite close to that in pure oxygen. To the best of our knowledge, this is the fastest conversion among any reported photocatalysts in air. Both a reactive oxygen species (ROS) quenching experiment and electron paramagnetic resonance (EPR) spectroscopy suggested that **PAF-68** rapidly initiated $^{\bullet}O_2^-$ rather than $^1O_2$. Compared to $^1O_2$, the generation of $^{\bullet}O_2^-$ is an oxygen concentration-independent process,[26–28] thus allowing a fast conversion rate without needing an atmosphere of pure oxygen. Different from ordered porous solids such as MOFs and COFs, the amorphous PAFs are a metal-free photocatalyst that initiates $^{\bullet}O_2^-$ as ROS. Mechanism investigation suggested that the porphyrin-based amorphous framework of **PAF-68** is a feature of low exciton binding energy and long decay lifetime when excited by light, both of which would facilitate the generation of $^{\bullet}O_2^-$. The tough carbon–carbon linkages of the PAFs hindered photodegradation of the skeleton, resulting in durable photocatalytic degradation performance even after several cycles. This work not only provides a promising material for the fast detoxication of mustard gas simulant in general environments, but also presents an innovative but inspiring design principle for the detoxication of chemical warfare agents with other types of ROS.

Results and discussion

Synthesis and characterization of PAF-68

Using photoactive **TBPP** and **EPA** as the building units, **PAF-68** was obtained under solvothermal conditions in the form of a purple powder. The structural characteristics of **PAF-68** were characterized by infrared spectroscopy (FT-IR), solid-state ^{13}C CP/MAS NMR and X-ray photoelectron spectroscopy. The FT-IR spectrum is shown in Fig. 2a. The peaks at 564 and 515 cm^{-1} are related to the stretching vibration of C–Br on the monomer **TBPP**, while the peak at 3281 cm^{-1} was attributed to the characteristic vibration from the terminal alkynyl C≡H bond in **EPA**. The fact that these characteristic peaks vanished in the product indicated that the building units had fully reacted, and the new, low-intensity peak at 2204 cm^{-1} was assigned to the stretching vibration peak of the newly formed alkyne bond in **PAF-68**. In the solid-state ^{13}C NMR, the chemical shift at around 90 ppm corresponds to the carbon–carbon triple bonds. Those at 118–152 ppm were assigned to aromatic carbons from the phenylporphine and phenylamine motifs in **PAF-68** (Fig. 2b). X-ray photoelectron spectroscopy (XPS) proved that **PAF-68** is metal-free and has two N 1s characteristic peaks of porphyrin and triphenylamine (Fig. S1†). Thus, the connection of the building units and the bonding mode of **PAF-68** could be confirmed as expected. Transmission electron microscopy (TEM) and scanning electron microscopy (SEM) were used to investigate the morphology of **PAF-68**. As can be observed in the SEM and TEM photographs (Fig. S2 and S3†), its morphology exhibited spherical nanoparticles with a size of 400–600 nm.

The permanent porosity of **PAF-68** was confirmed by N_2 adsorption analysis at 77 K. The N_2 adsorption–desorption isotherms of **PAF-68** showed a typical type I curve as predicted (Fig. 2c), and the hysteresis in the isotherms was attributed to the swelling of the entirely organic framework with increased pressure.[29] According to the Brunauer–Emmett–Teller model, the BET surface area of **PAF-68** was estimated to be 509 $m^2\ g^{-1}$. The total pore volume of **PAF-68** was 0.28 $cm^3\ g^{-1}$, with two primary pore diameters centered at 0.5 nm and 0.9 nm, respectively. The micropores facilitate substrate diffusion through the pores and provide accessibility to the reaction sites during catalytic conversion.

From the thermogravimetric analysis (TGA) curve (Fig. S4†) obtained under air flow, it is evident that the synthesized **PAF-68** showed almost no weight loss up to 400 °C. As the temperature rose further, a sharp decrease in weight was observed, which was attributed to decomposition of the skeleton. A chemical stability assessment was performed by porosity measurements on the **PAF-68** sample after stirring under harsh conditions and in organic solvents. The sample was either stirred in 3 M HCl (Fig. S5†) or 6 M KOH (Fig. S6†) for 48 h, or separately immersed in commonly used organic solvents, including tetrahydrofuran, methanol, dichloromethane, ethanol, and acetone for 24 h (Fig. S7†), then kept in ambient atmosphere for a whole year (Fig. S8†). The retained surface area indicated no obvious dissolution or degradation for **PAF-68**.

 © 2024 The Author(s). Published by the Royal Society of Chemistry

Open Access Article. Published on 27 August 2024. Downloaded on 2/7/2026 1:52:40 PM.
This article is licensed under a Creative Commons Attribution-NonCommercial 3.0 Unported Licence.

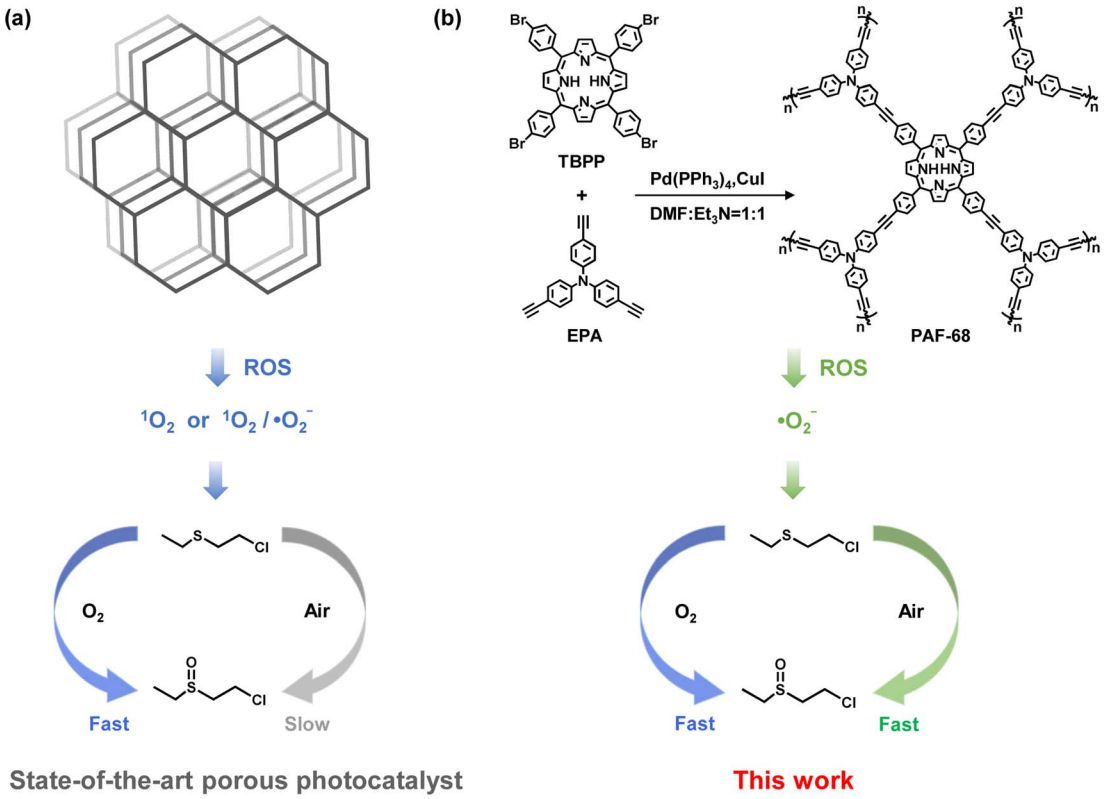

Fig. 1 (a) Previously reported porous photocatalysts for detoxification of mustard gas and simulants can ensure rapid oxidative degradation under pure oxygen, while the catalytic rate is greatly reduced in room air. (b) In contrast, **PAF-68** in this work degrades CEES in room air as fast as in pure oxygen.

Light absorption measurements were applied to understand the electronic energy band levels of **PAF-68**. The UV-Vis diffuse reflectance spectrum of **PAF-68** showed absorption bands in the wavelength range from 400 to 700 nm. The wide absorption band extends to the near-infrared region, which indicates its efficient light-harvesting ability due to the existence of the porphyrin macrocycle (Fig. 2d). A Kubelka–Munk-transformed reflectance spectrum based on UV-Vis DRS was recorded

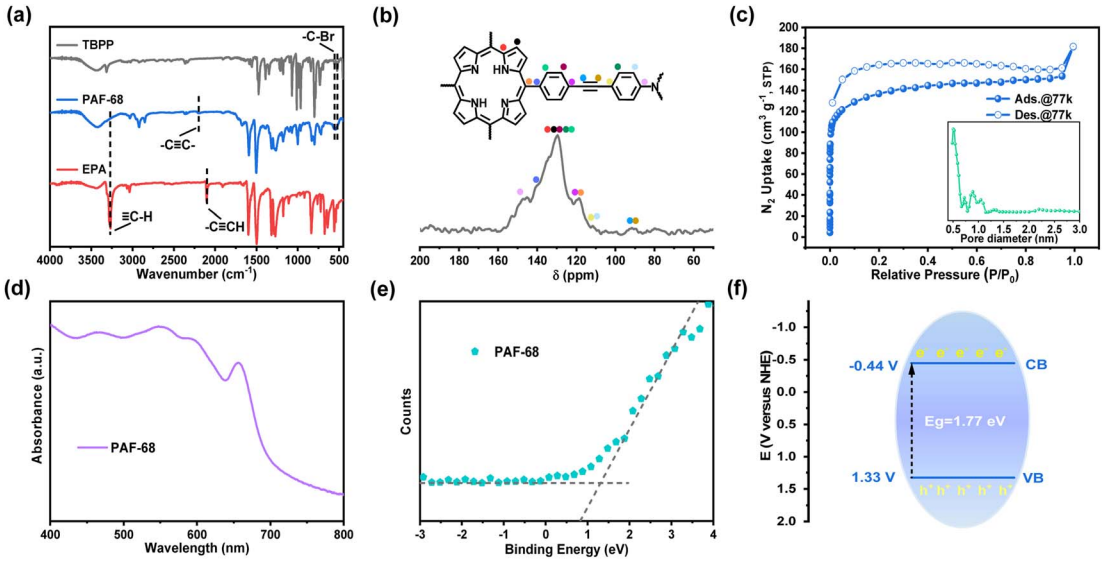

Fig. 2 Structural and optical characterization of **PAF-68**. (a) FT-IR spectra of **PAF-68**, **TBPP**, and **EPA** for comparison. (b) Solid-state ^{13}C CP/MAS NMR spectrum of **PAF-68**. (c) Nitrogen-sorption isotherm curves measured at 77 K and pore distribution of **PAF-68**. (d) UV-Vis DRS pattern of **PAF-68**. (e) VB-XPS spectrum of **PAF-68** (the VB positions of **PAF-68** are 1.33 eV below the Fermi level (EF)). (f) Band positions of **PAF-68**.

Open Access Article. Published on 27 August 2024. Downloaded on 2/7/2026 1:52:40 PM.
This article is licensed under a Creative Commons Attribution-NonCommercial 3.0 Unported Licence.

(Fig. S9†). According to the calculations derived from the Tauc plots, the corresponding optical bandgap (E_g) of **PAF-68** was estimated to be 1.77 eV, indicating that **PAF-68** is a semiconductor and possesses strong light-collecting capability. The valence band (VB) spectrum was also obtained using XPS for **PAF-68** to evaluate the energy band, and the VB potential was found to be 1.33 eV (Fig. 2e). Deducing from the experimental energy levels of E_g and VB, the conduction band (CB) was calculated to be −0.44 eV (Fig. 2f). The CB, with enough negative potential, provides multiple pathways for oxygen activation.

Photocatalytic activity of PAF-68

The porous structure and light response of **PAF-68** encouraged us to evaluate the catalytic oxidation of the toxic compounds, either in pure oxygen or in room air. CEES, a mustard gas simulant, was used as the modeling compound for safety reasons. The conversion and selectivity of the reaction were confirmed by ^{1}H NMR and ^{13}C NMR (Fig. 3a and S10†). In the ^{1}H NMR results, the chemical shifts at 1.24, 2.58, 2.85, and 3.65 ppm were assigned to CEES, and those at 1.35, 2.82, 2.92, 3.17, and 3.95 ppm were attributed to the expected product CEESO. Under the condition of pure oxygen, the chemical shifts from CEES gradually vanished, and those signals corresponding to CEESO began to appear as soon as CEES was injected (Fig. S11†). Fig. 3b showed that with the aid of **PAF-68**, CEES can be completely converted into the nontoxic oxidation product CEESO in 3.7 min. The half-life ($t_{1/2}$) for conversion of CEES to CEESO was evaluated to be 1.7 min, revealing the very fast degradation rate. It is noteworthy that although the detoxication process lasted for 2 h, no highly toxic 2-chloroethyl ethyl sulfone ($CEESO_2$) was detected at all, suggesting that CEESO was the only product, with a selectivity of 100% (Fig. S12†). As PAFs are highly stable with carbon–carbon linkages, the humid environment would not affect the photocatalytic activity of **PAF-68**. Even more, when pure oxygen flux was bubbled in water, the trace humidity from the atmosphere accelerated the catalytic reaction, and the half-life in humid oxygen was further accelerated to 1.5 min (Fig. S13†).

The oxygen content in room air environment is only 21% (*i.e.*, un-enriched in terms of oxygen). Under such a low oxygen partial pressure, the reported photocatalysts for CEES detoxification universally showed a significantly prolonged conversion half-life compared with oxidation in pure oxygen. For example, a porphyritic ligand-coordinated silver cluster exhibited a CEES degradation half-life of 1.5 min in pure oxygen, but the half-life of the same material in air was 6 min.[30] Another porphyrin-based MOF, Fe–TCPP–La, selectively converted CEES to CEESO with a half-life of 2.5 min in oxygen atmosphere, but in air the half-life was about 10 min.[14] Air atmosphere was also applied to **PAF-68** to further investigate the impact of oxygen concentrations on the conversion of CEES. Surprisingly, **PAF-68** exhibited selective conversion from CEES to CEESO in air almost as fast as in pure oxygen. Under an atmosphere of dry imitated air (N_2/O_2, v/v = 80, 20), CEES was fully converted into nontoxic CEESO within 7 min, with a $t_{1/2}$ of 2.4 min (Fig. S14†). Trace humidity from the atmosphere by gas bubbling also expedited the catalytic reaction, with the half-life reduced to 1.7 min (Fig. 3c and S15†). In a real room air atmosphere, **PAF-68** showed its wide suitability (Fig. S16 and S17†). Complete conversion from CEES to CEESO under humid air took 5.1 min, with a half-life of only 1.9 min (Fig. 3d). This conversion rate was comparable to that in imitated humid air ($t_{1/2}$ = 1.7 min)

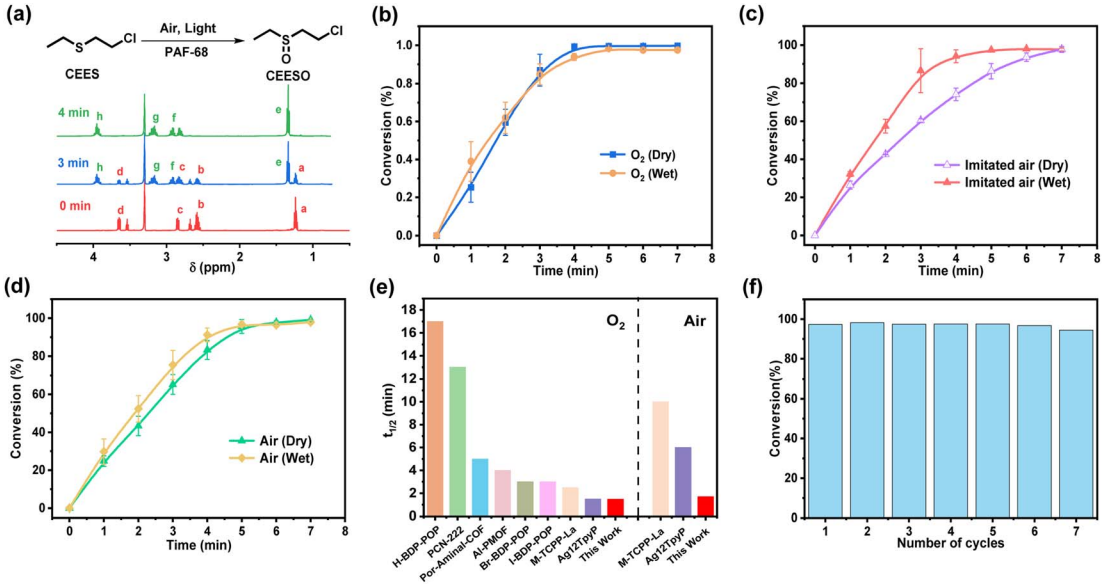

Fig. 3 Detoxification of CEES catalyzed by **PAF-68**. (a) Photooxidation reaction of CEES by **PAF-68** and ^{1}H NMR spectra measured 0 min, 3 min and 5 min before and after photooxidation. (b) Conversion of CEES in the presence of **PAF-68** under dry (blue) and wet (orange) pure O_2. (c) Conversion of CEES in the presence of **PAF-68** under dry (purple) and wet (red) simulated air. (d) Conversion of CEES in the presence of **PAF-68** under dry (green) and wet (yellow) room air. (e) The half-life of CEES degradation using **PAF-68** compared with other POP photosensitizers in pure oxygen and in air. (f) Recycling performance of **PAF-68** towards photooxidation of CEES.

 © 2024 The Author(s). Published by the Royal Society of Chemistry

Open Access Article. Published on 27 August 2024. Downloaded on 2/7/2026 1:52:40 PM. This article is licensed under a Creative Commons Attribution-NonCommercial 3.0 Unported Licence.

and humid oxygen ($t_{1/2}$ = 1.5 min). Even under an extremely low-oxygen condition (N_2/O_2, v/v = 98/2), CEES could still be completely converted to CEESO with a $t_{1/2}$ of 2.7 min (Fig. S18–S21†), further demonstrating that the catalytic effect of **PAF-68** is oxygen concentration-independent. Compared with other reported materials with greatly reduced conversion in air, the detoxification rate of **PAF-68** to CEES in air atmosphere is very close to that in pure oxygen (Fig. 3e and Table S1†).

The covalent carbon–carbon linkages also render their excellent chemical stability in PAFs over other MOF-based catalysts. **PAF-68** was used as a catalyst in humid air and recovered after the photocatalytic degradation. The results indicated that **PAF-68** retained similar conversion rate and selectivity after 7 cycles, equivalent to those of the original catalyst (Fig. 3f). The FT-IR, solid-state ^{13}C NMR, N_2 adsorption and XPS spectra indicated that cycled PAFs have unaltered structure and permanent porosity, and no CEES and CEESO residues (Fig. S22†). At the same time, after keeping **PAF-68** at room temperature in room air for a year, it still exhibited the same catalytic activity (Fig. S23†), indicating its structural stability and availability for long-term storage as well. For comparison, CEES detoxification was carried out without light and without **PAF-68**, respectively. The results showed that CEES did not convert within 15 min (Fig. S24†). When the reaction is carried out in aprotic solvents such as deuterated chloroform, $CEESO_2$ and the oxidation elimination product ethyl vinyl sulfoxide (EVSO) signals are detected, consistent with previous reports (Fig. S25†).[31] In order to prove the rapid detoxification caused by the superiority of **PAF-68** rather than the experimental conditions, a typical PCN-222 was synthesized and compared (Fig. S26–S28†). The results showed that under the same conditions, the half-life of CEES degradation by PCN-222 in pure oxygen was 27.2 min, and the half-life in air was 33.6 min, which was close to the previously reported white light conditions.

Mechanism investigation

As a metal-free organic photocatalyst, **PAF-68** generates ROS for fast decontamination of mustard gas simulant. It is rewarding to understand the generation of specific ROS for the corresponding photocatalytic process and shed light on the design of photocatalysts for CWA detoxification. In general, photocatalysts initiate the generation of different kinds of ROS such as $^{\bullet}O_2^-$, $^{\bullet}OH$, H_2O_2, and $^1O_2$ from molecular oxygen. To identify the type of ROS involved in this process, 1,4-benzoquinone, *tert*-butanol, catalase, and carotene were employed as quenching agents to selectively scavenge $^{\bullet}O_2^-$, $^{\bullet}OH$, H_2O_2, and $^1O_2$, respectively. Oxidation of 3,3′,5,5′-tetramethylbenzidine (TMB) was selected as an indicative reaction because colorless TMB is converted into the blue oxidized state (oxTMB) when exposed to light. As shown in Fig. 4a, the degree of oxidation was monitored by the characteristic UV-Vis absorption at 370 and 652 nm. The results were recorded and summarized in Fig. 4b. When 1,4-benzoquinone was used as the quenching agent for $^{\bullet}O_2^-$, the oxidation of TMB was completely prevented, leaving no color change of the TMB solution and no absorbance signal in UV-Vis. With regards to other trapping agents for $^{\bullet}OH$, H_2O_2, and $^1O_2$, quenching was not observed, indicating the absence of these ROS. Therefore, it is believed that $^{\bullet}O_2^-$ is the predominant ROS in the photocatalytic process initiated by **PAF-68**. Further convincing evidence for the identification of ROS was given by electron paramagnetic resonance spectroscopy (EPR). As a spin-trapping agent, 5,5-dimethyl-1-pyrroline-oxide (DMPO) was added to the photocatalysis reaction. Under light irradiation, four peaks were observed, and their appearance was attributed to the existence of DMPO*$^{\bullet}O_2^-$. The peaks were significantly weakened in the dark, indicating the initiation of $^{\bullet}O_2^-$ was driven by light irradiation (Fig. 4c). In contrast, there was no spin signal for $^{\bullet}OH$ or $^1O_2$ observed either under light irradiation or in darkness. (Fig. S29†). Together with the results of the quenching experiments, both of them showed that $^{\bullet}O_2^-$ was the predominant ROS in the photoinduced process involving **PAF-68**. Compared with other reported HD/CEES detoxication photocatalysts such as MOFs and COFs,[30,32] where $^1O_2$ is usually present as the main ROS, PAF materials exclusively generating $^{\bullet}O_2^-$ as ROS would be an exciting result for photocatalyst design and photodynamic therapy, as $^{\bullet}O_2^-$ is independent of the oxygen concentration. For this reason, there is merit in unveiling the reason for ROS generation by metal-free or entirely organic compounds.

Herein, we proposed a plausible reaction mechanism of the photocatalytic detoxification of CEES by **PAF-68** as shown in Fig. S30.† Under visible light excitation, **PAF-68** changes from the ground state to the excited state, producing photoinduced electrons and photoinduced holes. Subsequently, O_2 is activated by electron transfer to generate O_2^-. On the other hand, the hole combines with CEES to form a positively charged intermediate A. Intermediate A combines with O_2 to form peroxide B. Finally, peroxide B reacts with CEES to form the product CEESO. Quantum chemical calculations have been further conducted to explore the excited-state properties of **PAF-68** and get in-depth insights into the underlying mechanism of $^{\bullet}O_2^-$. Our calculations suggest (Fig. S31†) that the first electronically excited singlet state S_1 of **PAF-68** is of local π–π^* character, and thus is the vertical transition to the Franck–Condon point with the S_0 stable structure. S_1 state corresponds to the excitation of electrons from the two highest occupied molecular orbitals (HOMOs) to the two lowest unoccupied molecular orbitals (LUMOs), which can be explained by the Gouterman model (so-called four-orbital model).[33] The orbital contributions of HOMO to LUMO and HOMO−1 to LUMO+1 for S_0 to S_1 excitation account for 62.9% and 35.0%, respectively. We also revealed the excited-state relaxation process from the S_0 to T_1 states by optimizing the minima of the corresponding states and computing linearly interpolated internal coordinate paths. The corresponding relaxation pathway is depicted in Fig. 4d. Upon photoexcitation, **PAF-68** is vertically excited to the Franck–Condon point, and then relaxes rapidly to the S_1 minimum with the S_0–S_1 energy gap of 2.036 eV. Subsequently, PAF68 further decays to the T_2 intermediate state through the intersystem crossing process, with the S_1–T_2 energy gap of 0.486 eV. In T_2 state, PAF68 relaxes rapidly to its minimum, with the S_0–T_2 energy gap of 1.374 eV, and then goes on decaying to

Open Access Article. Published on 27 August 2024. Downloaded on 2/7/2026 1:52:40 PM.
This article is licensed under a Creative Commons Attribution-NonCommercial 3.0 Unported Licence.

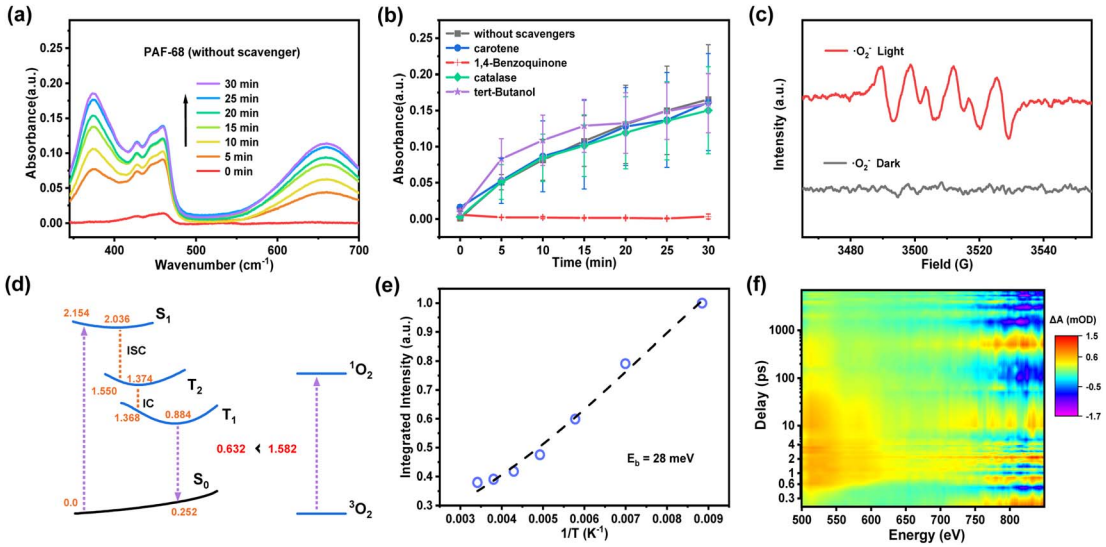

Fig. 4 Practicability and carrier dynamics of **PAF-68**. (a) Time-dependent UV-Vis absorption spectra of TMB oxidation over **PAF-68**. (b) **PAF-68** in the presence of different scavengers under visible light irradiation. (c) EPR spectra of **PAF-68** in the presence of DMPO. (d) Suggested excited-state relaxation pathway from the initially populated S_1 to T_1 states of **PAF-68** mediated by an intermediate T_2 state, and energy profile for the type-II energy transfer from the T_1 **PAF-68** to $^3O_2$. (e) Integrated PL intensity of **PAF-68** as a function of temperature from 83 K to 293 K. (f) fs-TA spectra of **PAF-68** following excitation at 400 nm.

the T_1 state followed by rapid internal conversion process from T_2 to T_1, with the T_2–T_1 energy gap of 0.006 eV. In the T_1 state, PAF68 relaxes to its minimum. The vertical T_1–S_0 emission energy was calculated to be 0.632 eV, which is significantly lower than the energy gap of 1.582 eV that is required to excite $^3O_2$ to its singlet excited state to produce $^1O_2$, indicating that this process could be endothermic. Therefore, in thermodynamics, the excitation energy transfer from the T_1 state of **PAF-68** to $^3O_2$ is not beneficial.

As the excitation energy transfer process is unfavorable, the other pathway to ROS would be a charge transfer process that generates $^{\bullet}O_2^{-}$. To understand the photoinduced electron–hole pair recombination and separation in **PAF-68**, the exciton-binding energy (E_b) was determined by temperature-dependent photoluminescence (PL) measurement. The PL intensity of **PAF-68** decreases rapidly with the increase of temperature from 83 K to 293 K (Fig. S32†). Arrhenius equation fitting of the integral PL intensity as a function of temperature indicated the E_b of **PAF-68** was about 28 meV (Fig. 4e), which is much lower than the values for typical polymers at about 100 meV. The low E_b of **PAF-68** is in favor of the formation of free electrons and thus facilitates the generation of $^{\bullet}O_2^{-}$. The thermal dissociation ratio was also calculated (Fig. S33†). It was recently reported that exciton dissociation at the order–disorder interfaces could be boosted by the simultaneous electron injection and hole blocking.[34] As PAFs are usually considered long-range disordered structures with local regularity, the unique structural feature of PAFs would be a possible reason for the low binding energy.

To further explore the excitonic processes involved in **PAF-68**, the photoexcited carrier kinetics in **PAF-68** was studied by femtosecond time-resolved transient absorption (fs-TA) spectroscopy in air at 298 K.[35,36] A 400 nm pump pulse was used to excite **PAF-68**. The two-dimensional pseudo-color (ΔA) plot in Fig. 4f was generated by fitting the transient absorption spectrum of **PAF-68** with the change of delay time and probe wavelength. As the global fitting analysis has been completed, the steady-state absorption spectrum was then obtained. A broad excited-state absorption over the range of 500–650 nm was attributed to the photoinduced absorption (PA) of electrons in **PAF-68** (Fig. S34†), which relates to the formation of free carriers.[37] The positive signal of **PAF-68** increases continuously at 522 nm before 0.6 ps, and the continuous absorption of **PAF-68** at 0.8 ps to 7.5 ns at 522 nm reflects the intramolecular charge transfer. The excited state decay after 516 nm optical excitation was plotted to further describe the lifetime of the photogenerated charge carriers. The fitting results showed that the average lifetime of the photogenerated charge of **PAF-68** was about 1017 ps (Fig. S35†). The long decay lifetime, which is in favor of effective electron–hole separation, is feasible in **PAF-68**. The delayed excited state decay results are consistent with low exciton binding energy, which excellently supports that **PAF-68** has a long-term carrier lifetime and effective exciton dissociation, and both facilitate the efficient generation of $^{\bullet}O_2^{-}$. These findings together support that the amorphous PAFs could affect ROS production, and eventually leading to their rapid catalytic detoxification of CEES in room air.

Conclusions

In summary, a porphyrin-based PAF was synthesized, and its photocatalytic decontamination of a mustard gas simulant was studied. Compared to other leading CEES detoxication catalysts, **PAF-68** rapidly degraded CEES to nontoxic CEESO in room air, with a $t_{1/2}$ of 1.7 min and a selectivity of 100%. The performance in air not only surpasses that of many

 © 2024 The Author(s). Published by the Royal Society of Chemistry

Open Access Article. Published on 27 August 2024. Downloaded on 2/7/2026 1:52:40 PM. This article is licensed under a Creative Commons Attribution-NonCommercial 3.0 Unported Licence.

photocatalysts under pure oxygen; it is also much desired due to the availability and safety of the oxidant supply. Mechanism investigation revealed that $^{\bullet}O_2^-$ was initiated as a ROS by photoactivated **PAF-68** and quickly detoxicated mustard gas simulant in room air. **PAF-68** has low exciton binding energy and a long decay lifetime, which are in favor of the generation of $^{\bullet}O_2^-$. Their stability and applicability in typical room air support PAFs as promising photocatalysts for CEES degradation in real-world environments, offering an original foundation for the future development of effective and widely applicable photocatalysts.

Data availability

The data supporting this article have been included as part of the ESI.†

Author contributions

J. S. and H. L. contributed equally to this work. G. Z. conceived the project. Y. T. and J. S. supervised the project. J. S., H. L. and Y. T. designed the experiments, analyzed the data, and wrote the manuscript. H. L. carried out most of the experiments. Y. Z., Y. D. and X. H. participated in photocatalysis tests. Z. D. participated in the TMB quenching experiment. F. C. provided the theoretical support. All authors discussed the results and commented on the manuscript.

Conflicts of interest

There are no conflicts to declare.

Acknowledgements

The authors are grateful for financial support from the Science and Technology Development Plan Project of Jilin Province, China (20240602105RC), China Postdoctoral Science Foundation (2024T170120, 2023M740577), National Natural Science Foundation of China (22131004, U21A20330, 22075040), the "111" project (B18012), Fundamental Research Funds for the Central Universities (2412023QD013), Postdoctoral Funding Project of Jilin Province, China.

References

1 K. Kim, O. G. Tsay, D. A. Atwood and D. G. Churchill, *Chem. Rev.*, 2011, **111**, 5345–5403.
2 Y. Liu, A. J. Howarth, N. A. Vermeulen, S.-Y. Moon, J. T. Hupp and O. K. Farha, *Coord. Chem. Rev.*, 2017, **346**, 101–111.
3 J. Dong, J. Hu, Y. Chi, Z. Lin, B. Zou, S. Yang, C. L. Hill and C. Hu, *Angew. Chem., Int. Ed.*, 2017, **56**, 4473–4477.
4 Y. Li, D. Zhang, W. Qiao, H. Xiang, F. Besenbacher, Y. Li and R. Su, *Chem. Synth.*, 2022, **2**, 9.
5 Y. Liu, A. J. Howarth, J. T. Hupp and O. K. Farha, *Angew. Chem., Int. Ed.*, 2015, **54**, 9001–9005.
6 C. T. Buru, M. C. Wasson and O. K. Farha, *ACS Appl. Nano Mater.*, 2020, **3**, 658–664.
7 A. Atilgan, M. M. Cetin, J. Yu, Y. Beldjoudi, J. Liu, C. L. Stern, F. M. Cetin, T. Islamoglu, O. K. Farha, P. Deria, J. F. Stoddart and J. T. Hupp, *J. Am. Chem. Soc.*, 2020, **142**, 18554–18564.
8 Q.-Y. Wang, J. Liu, M. Cao, J.-H. Hu, R. Pang, S. Wang, M. Asad, Y.-L. Wei and S.-Q. Zang, *Angew. Chem., Int. Ed.*, 2022, **61**, e202207130.
9 N. S. Bobbitt, M. L. Mendonca, A. J. Howarth, T. Islamoglu, J. T. Hupp, O. K. Farha and R. Q. Snurr, *Chem. Soc. Rev.*, 2017, **46**, 3357–3385.
10 Y. Hou, H. An, Y. Zhang, T. Hu, W. Yang and S. Chang, *ACS Catal.*, 2018, **8**, 6062–6069.
11 L. Ma, Y. Liu, Y. Liu, S. Jiang, P. Li, Y. Hao, P. Shao, A. Yin, X. Feng and B. Wang, *Angew. Chem., Int. Ed.*, 2019, **58**, 4221–4226.
12 J. P. Celli, B. Q. Spring, I. Rizvi, C. L. Evans, K. S. Samkoe, S. Verma, B. W. Pogue and T. Hasan, *Chem. Rev.*, 2010, **110**, 2795–2838.
13 L. Jiang, H. Bai, L. Liu, F. Lv, X. Ren and S. Wang, *Angew. Chem., Int. Ed.*, 2019, **58**, 10660–10665.
14 Z.-H. Long, D. Luo, K. Wu, Z.-Y. Chen, M.-M. Wu, X.-P. Zhou and D. Li, *ACS Appl. Mater. Interfaces*, 2021, **13**, 37102–37110.
15 Z.-X. Sun, K. Sun, M.-L. Gao, Ö. Metin and H.-L. Jiang, *Angew. Chem., Int. Ed.*, 2022, **61**, e202206108.
16 Y. Qian, D. Li, Y. Han and H.-L. Jiang, *J. Am. Chem. Soc.*, 2020, **142**, 20763–20771.
17 Y. Peng, Q. Tan, H. Huang, Q. Zhu, X. Kang, C. Zhong and B. Han, *Chem. Synth.*, 2022, **2**, 15.
18 Y. Tian and G. Zhu, *Chem. Rev.*, 2020, **120**, 8934–8986.
19 T. Ben, H. Ren, S. Ma, D. Cao, J. Lan, X. Jing, W. Wang, J. Xu, F. Deng, J. M. Simmons, S. Qiu and G. Zhu, *Angew. Chem., Int. Ed.*, 2009, **48**, 9457–9460.
20 A. A. Uliana, N. T. Bui, J. Kamcev, M. K. Taylor, J. J. Urban and J. R. Long, *Science*, 2021, **372**, 296–299.
21 Y. Ma, F. Cui, H. Rong, J. Song, X. Jing, Y. Tian and G. Zhu, *Angew. Chem., Int. Ed.*, 2022, **61**, e202113682.
22 J. Song, Y. Li, P. Cao, X. Jing, M. Faheem, Y. Matsuo, Y. Zhu, Y. Tian, X. Wang and G. Zhu, *Adv. Mater.*, 2019, **31**, 1902444.
23 J. Zou, A. Trewin, T. Ben and S. Qiu, *Angew. Chem., Int. Ed.*, 2020, **59**, 769–774.
24 Z. Li, L. Wang, M. Yu, Y. Liu, B. Liu, Z. Sun, W. Hu and G. Zhu, *ACS Appl. Mater. Interfaces*, 2022, **14**, 53798–53807.
25 Z. Zhang, Y. Zheng, Z. Dou, M. Gu, M. Sun, J. Song, N. Gao, F. Cui, Y. Tian and G. Zhu, *ACS Cent. Sci.*, 2023, **9**, 488–493.
26 M. Li, J. Xia, R. Tian, J. Wang, J. Fan, J. Du, S. Long, X. Song, J. W. Foley and X. Peng, *J. Am. Chem. Soc.*, 2018, **140**, 14851–14859.
27 J. An, S. Tang, G. Hong, W. Chen, M. Chen, J. Song, Z. Li, X. Peng, F. Song and W.-H. Zheng, *Nat. Commun.*, 2022, **13**, 2225.
28 W. Chen, Z. Wang, M. Tian, G. Hong, Y. Wu, M. Sui, M. Chen, J. An, F. Song and X. Peng, *J. Am. Chem. Soc.*, 2023, **145**, 8130–8140.
29 J. Jeromenok and J. Weber, *Langmuir*, 2013, **29**, 12982–12989.
30 M. Cao, R. Pang, Q.-Y. Wang, Z. Han, Z.-Y. Wang, X.-Y. Dong, S.-F. Li, S.-Q. Zang and T. C. W. Mak, *J. Am. Chem. Soc.*, 2019, **141**, 14505–14509.

Open Access Article. Published on 27 August 2024. Downloaded on 2/7/2026 1:52:40 PM.
This article is licensed under a Creative Commons Attribution-NonCommercial 3.0 Unported Licence.

31 Y. Hao, E. K. Papazyan, Y. Ba and Y. Liu, *ACS Catal.*, 2022, **12**, 363–371.
32 S. Wang, Q. Sun, W. Chen, Y. Tang, B. Aguila, Y. Pan, A. Zheng, Z. Yang, L. Wojtas, S. Ma and F.-S. Xiao, *Matter*, 2020, **2**, 416–427.
33 M. Gouterman, *J. Mol. Spectrosc.*, 1961, **6**, 138–163.
34 H. Wang, X. Sun, D. Li, X. Zhang, S. Chen, W. Shao, Y. Tian and Y. Xie, *J. Am. Chem. Soc.*, 2017, **139**, 2468–2473.
35 J. Hu, K. Xu, L. Shen, Q. Wu, G. He, J.-Y. Wang, J. Pei, J. Xia and M. Y. Sfeir, *Nat. Commun.*, 2018, **9**, 2999.
36 X. Zhang, K. Geng, D. Jiang and G. D. Scholes, *J. Am. Chem. Soc.*, 2022, **144**, 16423–16432.
37 Z. Chen, Q. Zhang and Y. Luo, *Angew. Chem., Int. Ed.*, 2018, **57**, 5320–5324.

 © 2024 The Author(s). Published by the Royal Society of Chemistry